Metallurgy and materials

# Lower corrosion resistance of the nitrocarburized layer formed on two supermartensitic stainless steel types

http://dx.doi.org/10.1590/0370-44672023770104

**Cesar Augusto Duarte Rodrigues**[1,5]
https://orcid.org/0000-0002-5339-0183
**Luiz Carlos Casteletti**[2,6]
https://orcid.org/0000-0001-9570-629X
**Frederico Augusto Pires Fernandes**[3,7]
https://orcid.org/0000-0003-0800-9264
**Carlos Alberto Picon**[4,8]
https://orcid.org/0000-0002-9965-2169
**Germano Tremiliosi-Filho**[1,9]
https://orcid.org/0000-0001-9162-3438

[1]Universidade de São Paulo - USP, Instituto de Química de São Carlos, São Carlos - São Paulo - Brasil.

[2]Universidade de São Paulo - USP, Departamento de Engenharia de Materiais e Manufatura, São Carlos - São Paulo – Brasil.

[3]Universidade Federal do ABC - UFABC, Centro de Engenharia, Modelagem e Ciências Sociais Aplicadas, São Bernardo do Campo – São Paulo – Brasil.

[4]Universidade Estadual Paulista Julio de Mesquita Filho - UNESP, Campus de Ilha Solteira, Departamento de Física e Química, Ilha Solteira – São Paulo – Brasil.

E-mails: [5]cesarduarterz@gmail.com, [6]castelet@sc.usp.br, [7]codoico@gmail.com, [8]capicone56@yahoo.com.br, [9]germano@iqsc.usp.br

## Abstract

The aim of this study was to verify the pitting corrosion behavior in the surface layers obtained by plasma nitrocarburizing at 400 and 450 °C/5 h on two types of super-martensitic stainless steel, namely micro-alloyed (Nb-SMSS) and unalloyed (SMSS). The results reveal that in all the nitrocarburized layers, a discontinuous, thin layer measuring less than 5µm in thickness exhibits a microhardness exceeding 950 $HV_{0.05}$, for the two steels. Furthermore, the structure of the surface layer is a combination of expanded austenite (γN), expanded martensite (α`N), ε-$Fe_{2-3}N$, cementite (θ-$Fe_3C$), and traces of CrN. The surfaces exhibit poor corrosion resistance across all layers, which can be attributed to localized micro-galvanic corrosion between the iron nitride (ε-$Fe_{2-3}N$) and expanded austenite (γN), since they are known to have higher corrosion resistance, as well as expanded martensite ((α`N) and cementite (θ-$Fe_3C$), which have lower corrosion resistance. This corrosion process initiates after the dissolution of the surface layer in a 3.5% NaCl solution, subsequently leading to substrate corrosion.

**Keywords:** super-martensitic stainless steel, plasma nitrocarburizing, pitting corrosion resistance, microstructure, hardness, niobium.

## 1. Introduction

It is well-known that supermartensitic stainless steel (SMSS) offers superior strength, toughness, weldability properties, and corrosion resistance when compared to conventional martensitic stainless steels like AISI-420 (Da Silva *et al*., 2012; Smith *et al*., 1999). These types of steel find wide application in various corrosive environments, such as chemical industries, pulp and paper industries, pollution control equipment, and the oil and gas industries for both onshore and offshore tubing (Bilmes *et al*., 2001; De-Ning *et al*., 2010;). The SMSSS chemical composition is based on the Fe-Cr-Ni-Mo system, with minimal levels of carbon, phosphorus, sulfur and nitrogen (C ≤ 0.02 wt. %, N ≤ 0.002 wt. % and P, S ≤ 0.003 wt. %) (Heimann, 2002; Toussaint, 2002). The ideal microstructure of these steels comprises a martensite matrix (90–95%) with a small percentage of retained austenite (1–10%) at micro and/or nanoscale sizes, and micro-alloying with Ti, Nb, and V in combination with C and N leads to the formation of carbon-nitride nanoprecipitates, which plays a crucial role in enhancing the material's mechanical and corrosion-resistant properties. Their pitting corrosion potential values range from 0.180 to 0.300 $V_{(SCE)}$ (Volden, 2008; Ma *et al*., 2013). When the nitrogen content is high (N > 0.002 wt.%), it promotes the precipitation of carbon nitrides (CN), and microalloying results in the formation of nitrides of type XN (X = Ti, Nb, V) and/or CrN in micro/nano sizes, which can reduce corrosion resistance (Lee, 2013; Ma, 2012).

Low-temperature plasma treatments, such as nitriding and nitrocarburizing, can significantly enhance the surface hardness and wear resistance of stainless steels without compromising their corrosion properties (Xi, 2008; Fernandes, 2013). Nitriding martensitic stainless steel at high temperatures for extended periods can lead to the precipitation of chromium carbides and/or nitrides within the layers, significantly reducing corrosion resistance (Kim, 2003; Allenstein, 2012). Plasma nitriding, gas nitriding and plasma immersion ion of martensitic precipitation hardening stainless steels (type 17–4 PH) improves the surface hardness, wear, and frictional properties (Mändl, 2005; Kochmański, 2008). Previous studies on SMSS involved the development, structural characterization, heat treatment, and mechanical and corrosion properties Rodrigues, *et al*., (2006; 2016). This study aims to investigate the pitting corrosion resistance of the nitrocarburized layer's microstructure in niobium-microalloyed SSMS (Nb-SMSS) and unalloyed steel (SMSS).

## 2. Experiment

Two SMSS types of steel were produced by the Villares Metals Research and Development Center (Villares Metals S.A., Brazil): SMSS microalloyed with niobium, referred to as Nb-SMSS, and unalloyed steel, referred to as SMSS. These steels present a high strength and toughness, as published by Rodrigues *et al*. (2006 and 2016). The chemical composition of the two steels, obtained through atomic absorption spectroscopy, is summarized in Table 1.

Table 1 - Chemical Compositions (Weight %) of Nb-SMSS and SMSS in the study.

| Sample | C | Cr | Ni | Mo | Mn | Si | S | Nb | P | N |
|---|---|---|---|---|---|---|---|---|---|---|
| Nb-SMSS | 0.019 | 12.50 | 5.36 | 2.10 | 0.31 | 0.21 | 0.005 | 0.20 | 0.005 | 0.001 |
| SMSS | 0.013 | 12.50 | 5.03 | 2.12 | 0.30 | 0.18 | 0.001 | - | 0.005 | 0.001 |

Two SMSS steel round bars with dimensions of 150 mm height and 29 mm diameter were heat treated: Nb-SMSS (1000 °C/45 min/water + 620 °C/2 h/air) and SMSS (1000 °C/45 min/water + 570 °C/2 h/air), then, cut it into wafer-shaped samples of 5 mm thickness and 14 mm diameter. All samples for structural characterization and plasma nitrocarburizing (PNC) treatments were prepared through progressive grinding with wet abrasive SiC sandpapers ranging from grit numbers 200 to 2000 and then polished using 20 µm chromium oxide powder. The SMSS microstructure was revealed by etching in "Vilella's" solution. The plasma nitrocarburized (PNC) treatment consisted of:, first, the samples were cleaned inside the plasma chamber by argon sputtering under a pressure of 500 Pa, at 50 °C lower than the treatment temperature for 30 min.; and second (PNC) treatments were carried out with the direct current (DC) method using a gas mixture (77 vol. % $H_2$, 20 vol. % $N_2$ and 3 vol. % $CH_4$), with a pressure of 500 Pa, at temperatures of 400 and 450 °C for 5 h (being these temperatures below the limit for the formation of retained austenite during tempering temperatures (~500 °C) Scheuer, *et al*. 2015). Hereafter, the PNC treated samples will be called SM400, SM450, Nb-SM400 and Nb-SM450, respectively. Pitting corrosion tests were carried out in 3.5 % NaCl solution, pH = 7.05, using an Autolab potentiostat (model PGSTAT-302). Experiments were performed using a classical three-electrode cell (capacity of 150 mL), a counter electrode of platinum foil of 2 $cm^2$, and the saturated calomel reference electrode (SCE). Firstly, the open-circuit potential (OCP) was measured during a rest time of 60 min for both compositions. However, after a first assessment, it was observed that for all samples, the OCP reached a steady-state value after 13 min. Therefore, a 15-minute interval was adopted as the stabilization time to achieve the OCP before starting the potentiodynamic polarization tests immediately after the immersion start. Also, the polarization curves were collected from from –1.0V vs. SCE up to – 1.2 V, at room temperature (25 °C ± 1 °C). All tests were carried out in duplicate. In this study, all corrosion potentials, corrosion current densities and pitting potential values for the different steels were calculated directly from the polarization curves (Pinedo, 2004). All microstructural analyses by optical microscopy (OM), model Zeiss – Axiotech, scanning electron microscope (SEM-LEO440) or (MEB-FEI-Magellan 400 L), coupled with an energy dispersive X-ray spectroscopy (EDS) system (EDS OXFORD ISIS LINK 300). X-ray diffraction (XRD) patterns were obtained from the surface of the samples in (XRD-Rigaku Rotaflex - Japan) using (Cu - Kα) radiation. The Vickers microhardness ($HV_{0.05}$) was measured in a Buehler 1600 instrument using a load of 50 gf for 10 seconds.

## 3. Results

### 3.1. Characteristics of SMSS samples

Microstructural analysis was observed through the cross-section, in the near-surface region of the SM400, SM450, Nb-SM400, and Nb-SM450 nitrocarburized layers, as shown in Figures (1a to 1c). In all the samples, a thin nitrocarburized layer can be observed on the top of the substrates, and below presents the martensitic matrix. In Figure 1(a), shows a discontinuous thin-layer, ranging from 2.0 to 3.0 µm, that is observed in the SM400 and SM450 layers, while in the Nb-SM400 and Nb-SM450 layers, the thickness varies between 2.0 to 5.0 µm, as shown in Figure 1 ((b) and (c)) and magnified by SEM image (representing the regions of Figure 1(c)). Moreover, the pores (micro defects), indicated by the white arrows in both Figure 1(a) and (b), show defects that are commonly observed in martensitic and nitrocarburized supermartensitic steels but not observed in other steel types, such as austenitic stainless steel. In this way, the occurrence of defects can occur due to the base steel composition

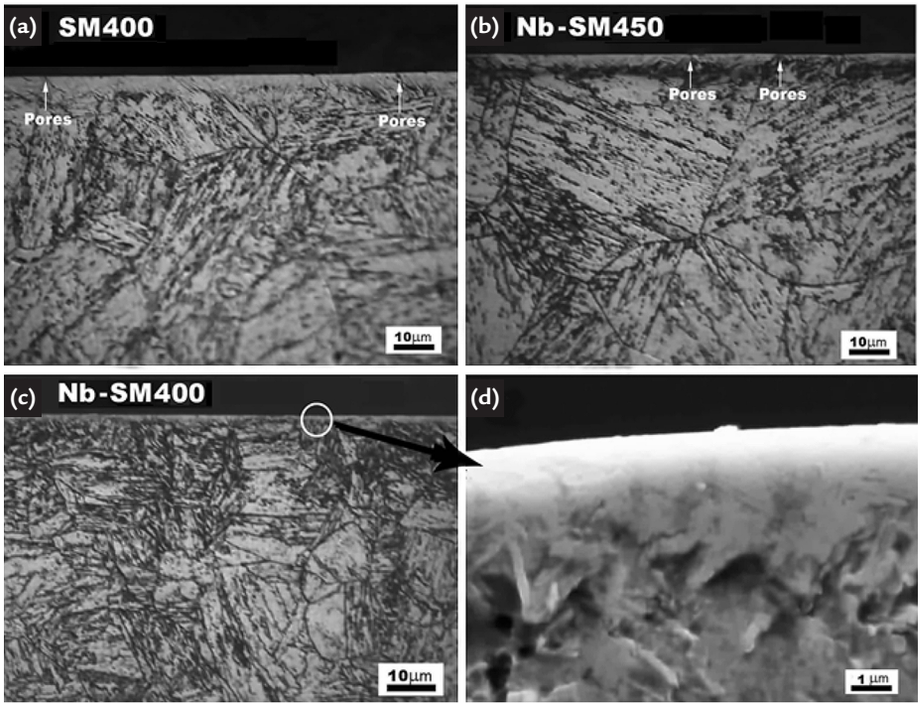


Figure 1 - OM images of (a) the SM substrate and SM400 layer, (b) the Nb substrate and Nb-SM450 layer, and (c) the Nb-SM substrate and Nb-SM400 layer. Also, (d) SEM image of the Nb-SM400 layer, representing regions magnified in Figure 1(c).

Figures 2 (a) and (b) show the X-ray diffraction (XRD) patterns obtained for the substrate, SM400, SM450, Nb-SM400, and Nb-SM450 nitrocarburized layers. The SM substrate (Figure 2(a)), shows the diffraction peaks of Fe-(α) and lower-intensity peaks of the retained austenite Fe-(γ). In contrast, the XRD pattern of the Nb-SM substrate (Figure 2(b)) exclusively presents the diffraction peaks of the martensite phase Fe-(α). In the SM400 layer, the primary peaks of iron carbide (θ-$Fe_3C$, cementite) were identified. These peaks overlap with those of iron nitride (ε-$Fe_{2-3}N$), expanded martensite (α`N), and expanded austenite (γN), albeit with lower intensities. Similarly, the SM450 layer exhibits the same diffraction peaks, but with slightly increased intensities (see Figure 2(a)). The Nb-SM400 layer exhibits peaks corresponding to iron carbide (θ-$Fe_3C$), (ε-$Fe_{2-3}N$), expanded martensite (α`N) and expanded austenite (γN), and expanded austenite (γN) with lower intensities; additionally, traces of the chromium nitride (CrN) phase were observed. On the other hand, the Nb-SM450 layer displays identical diffraction peaks with a slight increase in intensities (refer to Figure 2(b)).

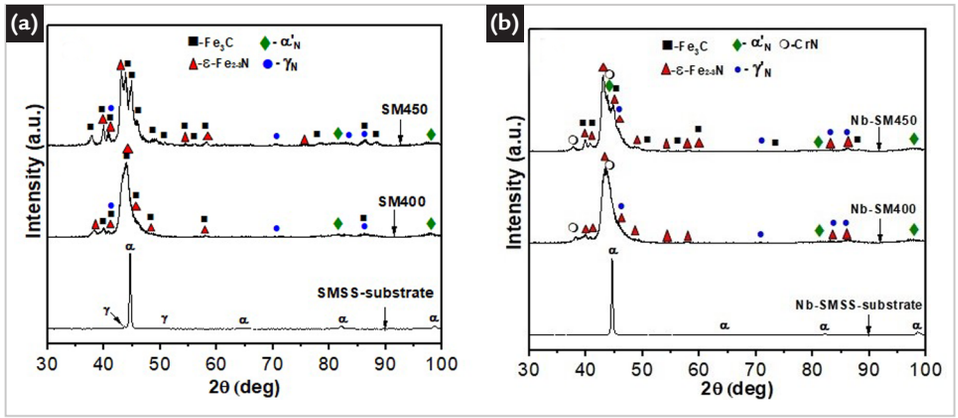


Figure 2 - X-ray diffraction patterns: (a) SM-substrate the SM400 layer and SM450 layers, and (b) Nb-SM-substrate, the Nb-SM450 layer and Nb-SM400 layers.

Figure 3(a) and (b) show the polarization curves for the nitrocarburized layers on SM400, SM450, Nb-SM400, Nb-SM450, and their respective SM-substrates in 3.5% NaCl. Figure 3 (a) shows the polarization curve of the SM-substrate, presenting a pitting potential of 0.40 $V_{(SCE)}$, while, for the SM400-layer of 0.0 $V_{(SCE)}$, and SM450-layer of –0.19 $V_{(SCE)}$, the SM400-layer exhibits two corrosion potential peaks at –0.47 $V_{(SCE)}$ and at –0.38 $V_{(SCE)}$ (1st and 2nd, as indicated in Figure 3 a), respectively. The first peak corresponds to the SM400-layer, accompanied by a slight decrease in both passive potential and passive current density. The emergence of the second peak is attributed to the breakdown of the SM400-layer surface, marking the initiation of the corrosion process on the substrate. Notably, the SM450-layer exhibits a single corrosion potential peak at –0.38 $V_{(SCE)}$.

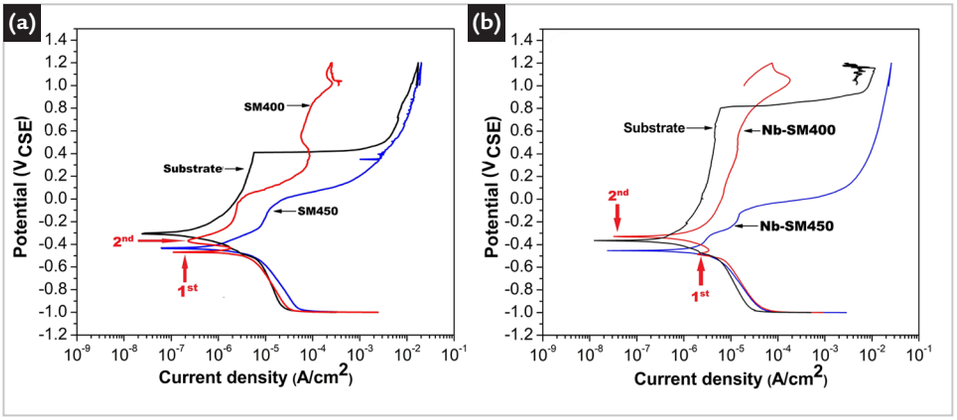


Figure 3 - Polarization curves determined in 3.5% NaCl: (a) SM-substrate, SM400 and SM450 layer, (b) Nb-SM-substrate, Nb-SM450 and Nb-SM400 layer.

Furthermore, the anodic curves of two layers, SM400 and SM450, exhibit a shift towards higher current densities, approximately half to one order of magnitude compared to the substrate anodic curve. In Figure 3(b), the anodic polarization curve of the substrate (Nb-SM) indicates a pitting potential of 0.80 $V_{(SCE)}$ and a corrosion potential of –0.37 $V_{(SCE)}$. In contrast, the Nb-SM450-layer displays a pitting potential of –0.40$V_{(SCE)}$ and a corrosion potential peak of –0.46 $V_{(SCE)}$.

The Nb-SM400-layer displays a pitting potential of 0.77 $V_{(SCE)}$, but it does exhibit two corrosion potential peaks at –0.48 $V_{(SCE)}$ and –0.33 $V_{(SCE)}$ (1st and 2nd, as indicated in Figure 3b). The first peak corresponds to the Nb-SM400-layer, marking the initiation of the passivation process with a sudden decrease in current density. Subsequently, the breakdown of the Nb-SM400-layer surface occurs in the first peak. The second peak corresponds to the substrate, indicating the beginning of the passivation process for the substrate. In contrast, the Nb-SM450-layer shows only a corrosion potential peak (–0.33 $V_{(SCE)}$) and undergoes rapid corrosion, depicting a typical profile of direct corrosion in the polarization curve. All values for the corrosion potential, pitting potential, and corrosion current density are provided in Table 2.

Table 2 - Summarizes the values of corrosion current density (Icorr), corrosion potential ($E_{corr}$), and pitting potential ($E_{pit}$), which are extracted from the polarization curves in Figure 3.

| Steel | $E_{corr}$ $V_{(SCE)}$ | $E_{pit}$ ($V_{(SCE)}$) | $I_c$ (A $cm^{-2}$) |
|---|---|---|---|
| **SM-Substrate** | –0.31 | 0.40 | $6.65 \times 10^{-8}$ |
| **SM400** | –0.43 | 0.00 | $1.20 \times 10^{-6}$ |
| **SM450** | –0.47 | –0.19 | $3.55 \times 10^{-7}$ |
| **Nb¬-SM-substrate** | –0.37 | 0.80 | $1.55 \times 10^{-7}$ |
| **Nb-SM400** | –0.33 | 0.77 | $4.70 \times 10^{-7}$ |
| **Nb-SM450** | –0.46 | –0.40 | $9.60 \times 10^{-7}$ |

## 4. Discussion

Microhardness ($HV_{0.05}$) measurements were directly taken on the nitrocarburized layers of SM400, SM450, Nb-SM400, and Nb-SM450 using optical micrographs along the layers. The results indicate that at elevated temperatures, the layer thickness in SM450 and Nb-SM450 leads to a slightly thicker case compared to SM400 and Nb-SM400 at similar temperatures. However, for both layers, a significant threefold increase in hardness is observed for all applied temperatures (microhardness of nitrocarburized layers closer to the top = 1131.80 for SMNb450, 1017.50 for SM400, 973.70 for Nb450, and 835.20 for SM400 in $HV_{0.05}$). These values sharply decrease with increasing depth (up to 20 µm), reaching the substrate hardness of 270 $H_{V0.05}$. It is widely recognized that iron-nitride (ε-$Fe_2$-$_3$N) demonstrates high hardness (exceeding 1100 HV), while chromium-nitride (CrN) exceeds 1200 HV. Other notable hardness values include expanded austenite-γN at approximately 850 HV, cementite-θ-$Fe_3C$ at around 800 HV, and expanded martensite-α`N at a slightly lesser hardness of approximately 550 HV (O'Brien, 1991; Allenstein, 2012). Therefore, all nitrocarburized layers exhibit elevated hardness levels attributed to the presence of the iron nitride and cementite phase mixture, as evident in the broad and overlapping XRD peaks (intensities are depicted in Figure 2 (a) and (b)).

In Figure 4 (a), (OM) images of the Nb-SM substrate reveal the presence of very fine retained austenite (a lighter-colored phase, measuring 0.5–1 µm) distributed along the boundaries of the martensite interlaths. Additionally, EDS scan line analysis of the Nb-SM substrate does not reveal significant changes in the Cr, Mo, and Ni contents (partitioning behaviors). The quantitative analysis by EDS over the retained austenite and martensite matrix (depicted in Figure 4 (a)), indicating weight percentages. In the martensite, the composition comprises 13.17 wt.% Cr, 4.97 wt.% Ni, 2.18 wt.% Mo, and 79.69 wt.% Fe. The retained austenite, on the other hand, exhibits concentrations of 13.16 wt.%

Cr, 5.49 wt.% Ni, 2.55 wt.% Mo, and 78.81 wt.% Fe. Notably, the elevated content of Ni atoms (5.49 wt.%) enriches the reversed austenite phase (Olson, 1985). Moreover, EDS scan line analysis of the Nb-SM400-layer, depicted in Figure 4 (b) (highlighted by the yellow arrow in Figure 4 (b), extending to a depth of 10 µm), reveals a composition of 30.42 wt.% C, 8.66 wt.% Cr, 3.99 wt.% Ni, 1.59 wt.% Mo, and 55.34 wt.% Fe. This composition indicates a higher carbon content in the top layer, which is reduced and stabilized with a uniform distribution. Conversely, there is an inverse behavior observed for the Cr and Ni elements. The clear detection of carbon atoms suggests that all carbon atoms are directed towards the formation of cementite (θ-$Fe_3C$).

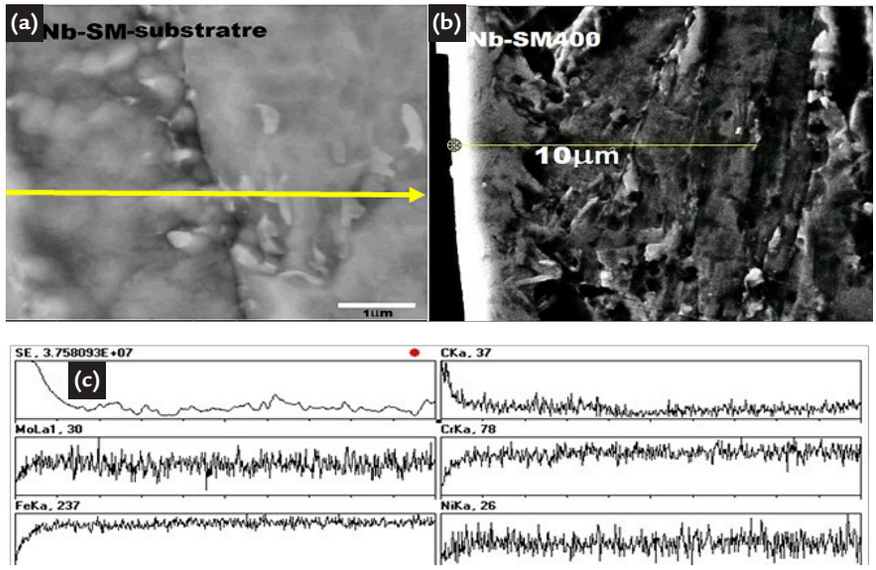


Figure 4 - (a) SEM image showcasing the retained austenite (lighter-colored phase) within the martensite grain boundaries of the Nb-SM substrate. (b) EDS line-scan profiles obtained along the yellow line to the Nb-SM400 layer. (c) Distribution of C, Mo, Fe, Ni, and Cr atoms along the analysed length (10 µm in depth).

This observation serves as a clear indicator that nitrogen atoms play a minimal role in the formation of iron nitride (ε-$Fe_{2-3}N$) and chromium nitride (CrN), with nitrogen present in significantly lower quantities. Notably, the nitrogen content in the substrate SMSS steel is exceptionally low (N= 0.001 wt. %). Nitrogen, well-known for its strong austenite-forming characteristics, thereby favors the creation of expanded austenite (γN) over expanded martensite (α'N) due to its low solubility in the martensite phase (Hamano, *et al.*, 2007; Ha, 2007). The presence of Ni, Cr, and Mo in both the martensite matrix and retained austenite indicates proximity to the stable chemical composition of the substrate (SM-Nb-steel). This composition exhibits high stability and possesses limited available C, Ni, Cr, and Mo atoms, which also limits the effective diffusion-reaction of nitrogen and carbon into the substrate interior. According to Kimura *et al.* (2001), retained austenite actively promotes the dissolution of carbon and nitrogen, and as a consequence, this phase acts as an obstacle in the continuous formation of a thicker layer. However, in contrast, Li Bell (2007) demonstrated that a nitrocarburized layer formed at 450°C for 20 hours on martensitic stainless steel comprises cementite (θ-$Fe_3C$) and iron nitride (ε-$Fe_{2-3}N$), whose composition presents clearly defined peaks of high intensities in the XRD pattern. In the case of the nitrocarburized layer, pitting curve behavior revealed a poor corrosion performance attributed to the presence of cementite (θ-$Fe_3C$) and traces of chromium carbide (CrC). Specifically, the nitrocarburized layer (SM450/5h and Nb-SM450/5h) with a shorter process time compared to Li & Bell (2007) treated at 20 hours resulted in a more efficient diffusion reaction of carbon compared to nitrogen at the elevated temperature of 450°C. Thus, efficiency favored the formation of cementite (θ-$Fe_3C$) which significantly reduced corrosion resistance, as in our case. It can be observed that the anodic polarization curve behavior indicates lower resistance, characteristic of direct corrosion, whereas the current density rapidly increases without the passivation process, revealing the pitting potential negative values. The poor pitting corrosion performance can primarily be ascribed to the presence of cementite (θ-$Fe_3C$), and includes the instability resulting from the phase mixtures of iron nitride (ε-$Fe_{2-3}N$), expanded martensite, and expanded austenite (α`N, γN), which react to each other in the form of coupled pairs; a phenomenon known for its propensity towards micro-galvanic corrosion. Moreover, under the nitrocarburized thin-layered discontinuous structure, the initial pitting process reaction tends to occur in the thinner regions, i.e., regions with high corrosion susceptibility. In their study, Basso *et al.*; 2009, explored the nitrocarburized layer on martensitic stainless steel (AISI-H13) at 2, 5, 7, 10, 15, and 20 hours at 563°C). The resulting structure layers were comprised of iron nitrides (ε-$Fe_{2-3}N$, γ'-$Fe_4N$) and CrN, with intensity peak redefinition of these phases, that increased with longer treatment times. However, for the short treatment time (2 hours), a thin layer (1–5 µm) formed, leading to diminished corrosion resistance, and longer treatment times (5 and 7 hours) resulting in a thicker layer (5–10 µm), significantly improving corrosion resistance in a NaCl solution. Interestingly, the structural morphology of the thin layer (1–5 µm) closely resembled the findings of our own study, as depicted in Figure 1 (d) through SEM observation. This similarity suggests a comparable behavior in terms of lower corrosion resistance in the nitrocarburized layers of SM450 and Nb-SM450 (thin-layered

< 3.0 µm) and SM400 and Nb-SM400 (thin-layered < 2.0 µm). Additionally, beneath the nitrocarburized layers, it was observed that all samples lacked distinct transition layers, signifying the absence of an evident diffusion zone. Particularly in martensitic stainless steels, where such transitional zones typically form due to the significant contribution of high carbon contents (>0.1% wt.), this characteristic has been previously characterized by other researchers (Alphonsa *et al*., 2002; Yan, 2010; Liu, 2010). The study of Fernandes *et al*. (2018), on the nitrocarburized SMSS steel at 400°C, 450°C, and 500°C, resulted in three distinct nitrocarburized layers, with similar results to our study, regarding terms of layers and phases formed. But, the intensity of these phase peaks presents an increase with rising temperature, paralleled by a corresponding increase in layer thickness (8µm at 400°C, 10µm at 450°C, and 27µm at 500°C). Moreover, the cementite phase in all nitrocarburized layers has been associated with lower corrosion performance, and the polarization curve behavior is found to be inferior compared to our study.

In Figure 5a and 5b, OM images depict the cross-sectional layers of Nb-SM400 and Nb-SM450 after corrosion tests. Figure 5 (a) specifically illustrates the morphology of the corroded surface in the Nb-SM400 layer, revealing the presence of micro-pits (highlighted by white arrows) scattered throughout the entire area. Notably, this layer underwent complete dissolution in the saline solution. The Nb-SM450 layer, as depicted in Figure 5b, reveals larger and more widely scattered pits across the entire observed area, indicative of rapid pitting corrosion. Similarly, the presence of numerous deep and larger pits was observed across the area, indicating rapid pitting corrosion, as illustrated in Figure 5 (c) SM400 and (d) SM450 samples. The corrosion aspects are shown in Figure 5 (e) Nb-SM400 and Figure 5 (f) Nb-SM450 samples. Lighter regions highlight where the pits initiate and expand, and corrosion morphology in Figure 5 (f) mirrors that of the SM400 and SM450 samples, respectively.

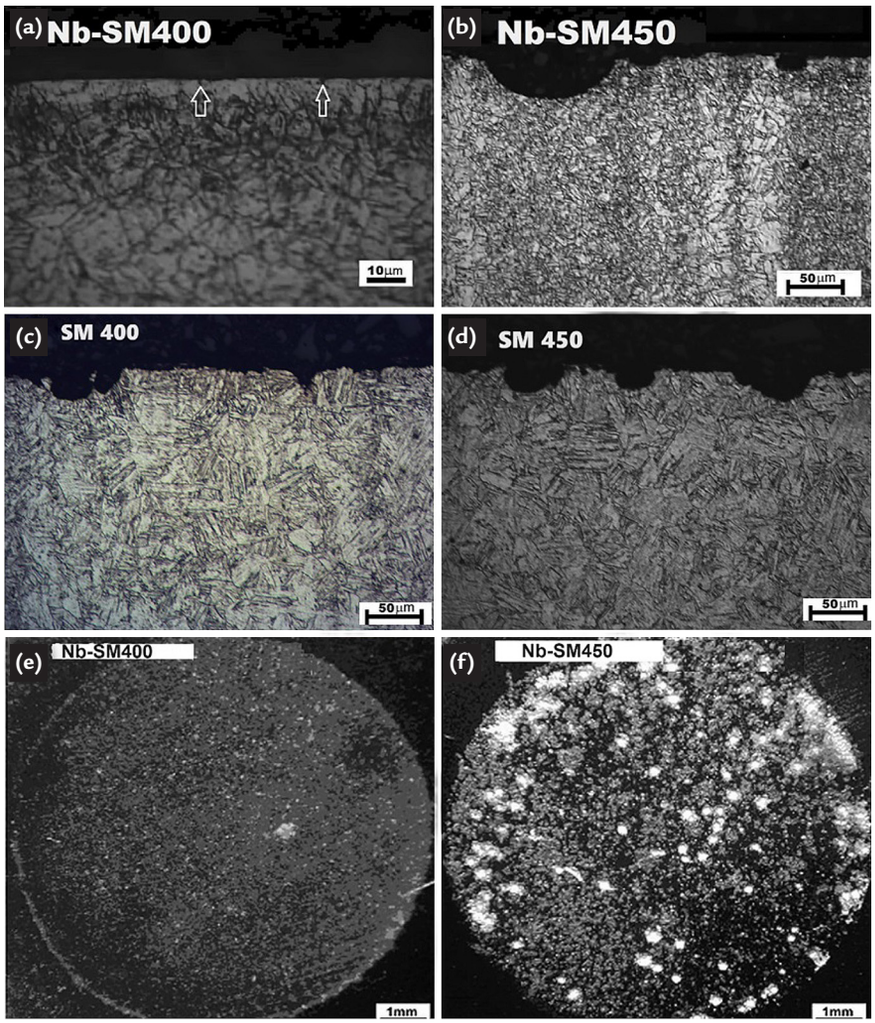


Figure 5 - OM images depicting cross-sectional layers of surfaces after pitting corrosion tests: (a) Nb-SM400, where the entire layer is dissolved in saline solution with the presence of micro-pits, and (b) Nb-SM450, characterized by larger and deeper pits along with complete layer dissolution and, similarly, (c) SM400 and (d) SM450 samples present larger and deeper pits along. The (e) Nb-SM400 and (f) Nb-SM450 samples show the surfaces corroded after corrosion tests.

## 5. Conclusions

The substrate's high stability, consisting of martensite and austenite with limited C and Cr atomic content, restricts the formation of a significant quantity of nitrides. Consequently, this hinders the growth of thicker layers, resulting in discontinuous and thin layers. In the nitrocarburized thin-layered structures of SM450 and Nb-SM450,

the predominant presence of cementite ($\theta$-$Fe_3C$) contributes to the rapid corrosion of these layers. The nitrocarburized thin-layered structures of SM400 and Nb-SM400 showcase phases, such as iron nitride ($\varepsilon$-$Fe_{2-3}N$) and expanded austenite ($\gamma N$), both characterized by higher resistance. However, the coexistence of martensite expanded ($\alpha`N$) and cementite ($\theta$-$Fe_3C$) with lower corrosion resistance in these structures, initiates a micro-galvanic reaction between these phases. This interaction results in rapid deterioration, particularly in regions with thinner layers.

## Acknowledgements

The authors are grateful to FAPESP, CAPES and CNPq (Brazil) for their financial supports. The authors CADR, RMB and GTF (Grant #2019/22183-6) acknowledge Fundação de Amparo à Pesquisa do Estado de São Paulo (FAPESP) for financial support. GTF (Grants # 313455/2021-0 and #408069/2022-8) and CADR (Grant # 380779/2023-4) are grateful to Conselho Nacional de Desenvolvimento Científico e Tecnológico (CNPQ) for scholarship and financial support. (Carmén Rodríguez de Duarte, 11/21/1933 – 01/04/2015).

## References

ALLENSTEIN, A. N.; LEPIENSKI, C. M.; BUSCHINELLI, A. J. A.; BRUNATTO, S. F. Plasma nitriding of CA-6NM steel: effect of $H_2$ + $N_2$ gas mixtures in nitride layer formation for low $N_2$ contents at 500 °C. ***Materials Research,*** v. 13/4, p. 557-562, 2010.

BASSO, R. L. O.; CANDAL, R. J.; FIGUEROA, C. A.; WISNIVESKY, D.; ALVAREZ, F. Influence of microstructure on the corrosion behavior of nitrocarburized AISI H13 tool steel obtained by pulsed DC plasma. ***Surface and Coatings Technology,*** v. 203, p. 1293-1297, 2009.

BILMES, P. D.; BILMES, SOLARI, M.; LLORANTE, C. L. Characteristics and effects of austenite resulting from tempering of 13Cr–NiMo martensitic steel weld metals. ***Materials Characterization***, v. 46, p. 285- 296, 2001.

DA SILVA G. F.; TAVARES S. S. M.; PARDAL J. M.; SILVA M. R. S and DE ABREU H. F. G. Influence of heat treatments on toughness and sensitization of a Ti-alloyed supermartensitic stainless steel. ***Materials Science and Engineering,*** 46, p 7737-7744, 2011.

DE-NING, Z.; YING, H.; WEI, Z.; XU-DONG, F. Influence of tempering process on mechanical properties of 00Cr13Ni4Mo supermartensitic stainless steel. ***Journal Iron and Steel Research, International***, v. 17, n. 8, p. 50-54, 2010.

FERNANDES, F. A. P.; L. CASTELETTI, L. C.; GALLEGO, J. Microstructure of nitrided and nitrocarburized layers produced on a superaustenitic stainless steel. ***Journal of Materials Research and Technology,*** v. 2, n. 2, p. 158-164, 2013.

FERNANDES, F. A. P.; PICONE, C. A.; TOTTEN, G. E.; CASTELETTI, L. C. Corrosion behavior of plasma nitrided and nitrocarburized supermartensitic stainless steel. ***Materials Research,*** v. 21, p. 1-9, 2018.

HA, H. Y.; KWON, H. S. Effects of $Cr_2N$ on the pitting corrosion of high nitrogen stainless steels. ***Electrochemical Acta,*** v. 52, p. 2175-2180, 2007.

HAMANO, S.; SHIMIZU, T.; NODA, T. Properties of low carbon high nitrogen martensitic stainless steels. ***Materials Science Forum,*** v. 539-543, p. 4975-4980, 2007.

HEIMANN, W.; LADWEWEIN, T.; NIROSTA, G. A systematic evaluation of the microstructure of 13 % chromium steels. *In*: Proceedings of the CONFERENCE ON SUPERMARTENSITIC STAINLESS STEELS, Bruxelas, p. 03-09, 2002.

KIMURA, M.; MIYATA, Y.; TOYOOKA, T.; KITAHABA, Y. Effect of retained austenite on corrosion performance for modified 13% Cr steel pipe. ***Corrosion,*** v. 57, n. 5, p. 433-439, 2001.

KOCHMAŃSKI, P.; NOWACKI, J. Influence of initial heat treatment of 17-4 PH stainless steel on gas nitriding kinetics. ***Surface and Coatings Technology,*** v. 202, p. 4834-4838, 2008.

LEE, S. H.; KAKATI, N.; MAITI, J.; JEE, S. H.; KALITA, D. J.; YOON, Y. S. Corrosion and electrical properties of CrN- and TiN-coated 316L stainless steel used as bipolar plates for polymer electrolyte membrane fuel cell. ***Thin Solid Films,*** v. 529, p. 374-379, 2013.

LI, C. X.; BELL, T. Corrosion properties of plasma nitrided AISI 410 martensitic stainless steel in 3.5% NaCl and 1% HCl aqueous solutions. ***Corrosion Science,*** v. 48, p. 2036-2049, 2006.

LI, X. L.; BELL, T. A comparative study of low temperature plasma nitriding, carburising and nitrocarburising of AISI 410 martensitic stainless steel. ***Surface and Coatings Technology,*** v. 23, n. 3, p. 355-361, 2007.

LIU, R.L.; YAN, M. F. The microstructure and properties of 17-4PH martensitic precipitation hardening stainless steel modified by plasma nitrocarburizing. ***Surface and Coatings Technology,*** v. 204, p. 2251-2256, 2010.

MA, X.; ZHOU C.; WANG, L.; LIU, C.; SUBRAMANIAN, S.; PEREZ DE OLIVEIRA, M. Role of Nb in low interstitial 13Cr supermartensitic stainless steel. ***REM - Revista Escola de Minas,*** v. 66, n. 2, p. 179-185, 2013.

O'BRIEN, J. M.; GOODMAN, D. Plasma (Ion) nitriding of steels, *In*: ***ASM Handbook.*** ASM International, Materials Park, Ohio, v. 4, 1991, 944 p.

OLSON, D. L. Prediction of austenitic weld metal microstructure and properties. ***Welding Research Suplement***, v. 64, p. 281-295, 1985.

PINEDO, C. E.; MONTEIRO, W. A. On the kinetics of plasma nitriding a martensitic stainless steel type AISI 420. ***Surface and Coatings Technology,*** v. 179, p. 119-123, 2004.

RODRIGUES, C. A. D.; DI LORENZO, P. L.; SOKOLOWSKI, A.; BARBOSA, C. A.; ROLLO, J. M. D. A. Development of a Supermartensitic Stainless Steel Microalloyed with Niobium. ***Journal of ASTM International,*** v. 3, p. 233-236, 2006.

RODRIGUES, C. A. D.; BANDEIRA, R. M.; DUARTE, B. B.; TREMILIOSI-FILHO, G. Effect of phosphorus content on the mechanical, microstructure and corrosion properties of supermartensitic stainless steel, A. M. Jorge. ***Materials Science and Engineering,*** A 650, p. 75-83, 2016.

SCHEUER, C. J.; CARDOSO R. P.; BRUNATTO S. F. Low-temperature plasma assisted thermochemical treatments of AISI 420 steel: comparative Study of Obtained Layers. ***Materials Research***, v. 18, n. 6, p. 1392-1399, 2015.

SMITH L.M.; CELANT W. Martensitic stainless flowlines: do they pay? *In*: CONFERENCE SUPERMARTENSITIC STAINLESS STEELS, p. 66-73, 1999. ***Proceedings*** **[...]**.

SUN, Y.; BELL. T. Low temperature plasma nitriding characteristics of precipitation hardening stainless steel. ***Surface Engineering,*** v. 19, p. 331-336, 2003.

TOUSSAINT, P.; DUFRANE, J. J. Advances in the making and base materials of supermatensitic stainless steels-SSMS. *In*: CONFERENCE SUPERMARTENSITIC STAINLESS STEELS, Bruxelas, p. 23 – 27, 2002. ***Proceedings*** **[...].**

VOLDEN, V.; THAULOW, C.; JOHNSEN, R. Modelling of hydrogen diffusion and hydrogen induced cracking in supermartensitic and duplex stainless steels. ***Materials & Design,*** v. 29, p. 1934-1948, 2008.

XI, Y. T.; LIU, D. X.; HAN, D. Improvement of corrosion and wear resistances of AISI 420 martensitic stainless steel using plasma nitriding at low temperature. ***Surface and Coatings Technology,*** v. 202, p. 2577-2583, 2008.

YAN, M. F.; LIU, R. L. Martensitic stainless steel modified by plasma nitrocarburizing at conventional temperature with and without rare earths addition. ***Surface and Coatings Technology,*** v. 205, p. 345-349, 2010.

Received: 31 August 2023 - Accepted: 16 January 2024.